

# Near-infrared spectroscopy of RS Ophiuchi in 2021: the calm, the storm, and the abatement

C. E. Woodward,<sup>1\*</sup> A. Evans,<sup>2†</sup> D. P. K. Banerjee<sup>3</sup>, B. Kaminsky<sup>4</sup>, S. Starrfield<sup>5</sup>, K. L. Page<sup>6</sup>, R. M. Wagner<sup>7,8‡</sup>

<sup>1</sup>Minnesota Institute for Astrophysics, University of Minnesota, 116 Church Street SE, Minneapolis, MN 55455, USA

<sup>2</sup>Astrophysics Research Centre, Lennard Jones Laboratory, Keele University, Keele, Staffordshire, ST5 5BG, UK

<sup>3</sup>Physical Research Laboratory, Navrangpura, Ahmedabad, Gujarat 380009, India

<sup>4</sup>Main Astronomical Observatory, Academy of Sciences of the Ukraine, Golosiiv Woods, UA-03680 Kyiv-127, Ukraine

<sup>5</sup>School of Earth and Space Exploration, Arizona State University, Box 876004, Tempe, AZ 85287-6004, USA

<sup>6</sup>School of Physics and Astronomy, University of Leicester, University Road, Leicester LE1 7RH, UK

<sup>7</sup>Department of Astronomy, The Ohio State University, 140 W. 18th Avenue, Columbus, OH 43210, USA

<sup>8</sup>Large Binocular Telescope Observatory, 933 North Cherry Avenue, Tucson, AZ 85721, USA

Accepted XXX. Received YYY; in original form ZZZ

## ABSTRACT

We present near-infrared (NIR) observations of the 2021 eruption of the recurrent nova RS Ophiuchi. The dataset provides both pre- and post-eruption perspectives on the eruption, as well as NIR spectra at high cadence. The spectrum obtained in 2020 June (14.3 years after the 2006 eruption, and 428.1 days before the 2021 eruption), is that of the red giant secondary, on which are superimposed several emission lines which most likely arise in the red giant wind. Spectra obtained during the eruption consist of emission (including coronal) lines, superimposed on a bremsstrahlung continuum at 8900 K. The temperature of the coronal gas is estimated to be  $10^{6.0}$  K on day 11.7, and  $10^{5.9}$  K on day 31.7. The high cadence observations, obtained on day 31.7 of the eruption, provide no conclusive evidence for rapid ( $\lesssim 1$  minute) variations in the He I 1.0833  $\mu\text{m}$  line. Data obtained about one year after the eruption show that there may have been changes in the spectral type of the secondary after the 2021 eruption.

**Key words:** circumstellar matter – stars: individual: RS Ophiuchi – novae, cataclysmic variables – infrared: stars

## 1 INTRODUCTION

RS Ophiuchi is the best studied of the symbiotic recurrent novae (SyRNe). It is a semi-detached binary consisting of a M0/2III red giant (RG) secondary with mass  $M_{\text{RG}} = 0.68 - 0.80 M_{\odot}$ , and a white dwarf (WD) primary with mass  $M_{\text{WD}} = 1.2 - 1.4 M_{\odot}$ ; its orbital period is 453.6 days (see Brandi et al. 2009, for details). The orbital inclination is estimated to be  $i = 49^{\circ} - 52^{\circ}$ , while  $a \sin i = 0.77$  AU, where  $a$  is the semi-major axis (Brandi et al. 2009). Using the formulae in Eggleton (1983), the radius  $R_{\text{RL}}$  of the RG’s Roche lobe is  $7.0 \times 10^{12}$  cm for these orbital parameters.

The RG has a wind, with estimated mass-loss rate  $\dot{M} \simeq 10^{-7} M_{\odot} \text{ yr}^{-1}$  and terminal velocity  $|V_{\text{w}}| = 18 \text{ km s}^{-1}$ ; these values are based on observations of narrow H $\alpha$ ,  $\beta$  emission lines over an orbital period (Somero, Hakala & Wynn 2017). The wind velocity determined by Somero et al. is consistent with that for field M2 giants (Wood, Müller & Harper 2016), for which the stellar radius  $R_{*} = 60.5 R_{\odot}$  ( $4.2 \times 10^{12}$  cm; van

Belle et al. 1999). This is comparable with the equivalent radius of the RG’s Roche lobe; however, whether or not the RG in symbiotic systems fills the Roche lobe remains a matter of debate (see, e.g. Boffin & Merc 2025; Merc & Boffin 2025).

Following the 2006 eruption, emission by silicate dust was reported by Evans et al. (2007c) and Woodward et al. (2008). The mass-loss rate inferred by the presence of silicates is  $1.0 - 1.7 \times 10^{-7} M_{\odot} \text{ yr}^{-1}$  (Rushton et al. 2022), consistent with the optical spectroscopy reported by Somero et al. The presence of a strong 18  $\mu\text{m}$  silicate feature indicates that it is not newly-formed: it has been in the RS Oph circumstellar environment for a considerable time and has survived many SyRN eruptions.

RS Oph is known to have undergone eight previous eruptions, in 1898, 1907(?), 1933, 1945(?), 1958, 1967, 1985, and 2006, those marked “(?)” being possible eruptions (Anupama 2008). The 1985 (Bode 1987) and 2006 (Evans et al. 2008) eruptions were particularly well studied, and observed over a wide wavelength range, from X-rays to radio.

The eruptions are the consequence of a thermonuclear runaway (TNR) on the surface of the WD, following mass transfer through the inner Lagrangian point on to the surface of

\* E-mail: chickw024@gmail.com

† E-mail: a.evans@keele.ac.uk

‡ Deceased.

the WD. There has been some discussion as to whether accretion onto the WD occurs via Roche lobe overflow (Azzollini et al. 2023) or via the RG wind (e.g., Walder, Folini & Shore 2008; Bollimpalli, Hameury & Lasota 2018). When conditions at the base of the accreted layer are suitable, the TNR ensues, leading to the eruption and the explosive ejection of  $\sim 10^{-7} - 10^{-6} M_{\odot}$  of material, at several  $1000 \text{ km s}^{-1}$ .

The ejected material encounters the RG wind, shocks it, and a reverse shock is driven into the ejecta. These events heat the ejected gas and RG wind to temperatures approaching  $10^6 \text{ K}$ , giving rise to coronal line emission in the ultraviolet, optical, and infrared, and to X-ray emission (Azzollini et al. 2023). The shocks also result in particle acceleration, and the production of non-thermal radio emission (Chomiuk, Metzger & Shen 2021). In many respects, observing the eruption of a SyRN like RS Oph is like observing the evolution of a supernova remnant, but in fast-forward. The fact that the WD mass (estimated to lie in the range  $1.2\text{--}1.4 M_{\odot}$ ; Brandi et al. 2009) is close to the Chandrasekhar limit, and is of CO type (Mikołajewska & Shara 2017), makes RS Oph particularly interesting from a Type Ia supernova progenitor perspective, and hence all the more fascinating.

The eruptions of 1985 (Evans et al. 1988) and 2006 (Das, Banerjee & Ashok 2006; Evans et al. 2007a,b,c; Banerjee, Das & Ashok 2009) were intensively observed in the infrared. We present here infrared spectroscopy of the 2021 eruption, from roughly one year before, to roughly one year after, the eruption.

## 2 THE 2021 ERUPTION

The 2021 eruption was discovered independently by K. Geary (August 8.93 UT) and A. Amorim (August 8.91; Geary & Amorim 2021); see Beck (2021) for a compilation of early observations. Munari & Valisa (2021) estimated that the eruption occurred on 2021 August 08.50 (MJD 59434.50). We take this to define the origin of time,  $t_0$ . The visual magnitude at discovery was 5.0.

The eruption was observed over the entire electromagnetic spectrum, including  $\gamma$ -rays (Cheung et al. 2022; Abe et al. 2025; Phan et al. 2025), X-rays (Page et al. 2022; Orio et al. 2022, 2023; Ness et al. 2023; Islam et al. 2024), and radio (Munari et al. 2022; de Ruiter et al. 2023; Lico et al. 2024; Nayana et al. 2024). Comprehensive optical spectroscopy is described by Munari & Valisa (2021, 2022) and Tomov et al. (2023). These observations showed outflows with velocities up to  $3500 \text{ km s}^{-1}$ .

Optical spectropolarimetry is given by Nikolov et al. (2023), who concluded that dust was present in the RS Oph system as early as day 2 of the eruption, but was destroyed between days 2 and 9. However, (presumably newly-formed) dust appeared at  $\gtrsim 80$  days into the eruption. If this is the case, RS Oph becomes the second SyRN in which dust formation occurred during an eruption (the first being V745 Sco; Banerjee et al. 2023). Nikolov et al. found that, at all times, the dust in RS Oph was asymmetrically distributed.

The X-ray evolution of the 2021 eruption is described by Page et al. (2022). The Super Soft Source (SSS) phase first appeared on day 20.6, and a soft component was clearly present on day 26.3; it persisted until at least day 63. X-ray observations of the 2006 eruption revealed 35 s quasi-periodic

oscillation (QPO) during the SSS phase (Beardmore et al. 2008; Nelson et al. 2008; Osborne et al. 2011). These QPOs were also seen during the 2021 eruption, although the X-ray evolution was quite different in the two eruptions (Page et al. 2022). The QPOs were present from days 36.9–61.6 during the 2021 eruption.

We assume reddening  $E(B-V) = 0.73$  (Snijders 1987), and the extinction law of Cardelli, Clayton & Mathis (1989) with a total-to-selective extinction value of 3.1. Historically, the distance of RS Oph has been taken to be  $D \simeq 1.6 \text{ kpc}$  (Bode 1987; Barry et al. 2008). More recently, however, Schaefer (2022) has given a somewhat larger distance ( $2710^{+198}_{-135} \text{ pc}$ ) based on Gaia data. We assume  $2.71 \text{ kpc}$  here.

## 3 OBSERVATIONS

### 3.1 IRTF

Spectra of RS Oph were obtained with SpeX (Rayner et al. 2003) on the 3.2 m NASA Infrared Telescope Facility (IRTF). The SpeXTool pipeline (Cushing, Vacca & Rayner 2004) was used to reduce these data, and to apply corrections for telluric absorption(s). The spectra were flux calibrated using an A0 standard star (HD 171149) observed at a comparable airmass ( $\Delta_{\text{AM}} \lesssim 0.15$ ). The IRTF flux calibrations are accurate to  $\pm 10\%$ . The resolving power corresponds to a velocity of  $250 \text{ km s}^{-1}$ . The observational log is presented in Table 1.

We use

$$T_{\text{conj}} = \text{MJD } 45\,043.04 + 453.6E, \quad (1)$$

where  $T_{\text{conj}}$  is the epoch of RG conjunction (Brandi et al. 2009), to determine the orbital phase for our observations (see Table 1). Note that all but one of our observations were obtained close to quadrature; the exception is the observation of 2023 April 22, obtained when the RG was at inferior conjunction. We therefore expect that, with the exception of the observation of 2023 April, the RG will be subject to some irradiation by the WD during the quiescent observations,

SpeX SXD\_K short spectra at high cadence using a  $0.5'' \times 15''$  slit also were obtained on day 31.7, shortly after the commencement of the SSS phase. All spectra were obtained in the "A-beam" (no ABBA nodding), and were reduced through the standard SpeX pipeline with the AOV star HD 171149 as the telluric calibrator. The first seven time series spectra had a cadence of  $\sim 14.4 \text{ s}$  (consisting of a 1.853 s exposure, 3 coadds, detector read-out, and file write to disk), while the 40 spectra were obtained with a  $\sim 6.0 \text{ s}$  cadence (single 1.853 s exposures plus overheads). The airmass for the first and last of the latter set differed by only 0.005, the entire set being obtained at airmass 1.150. During the high cadence observations, there were some clouds but it was clear in the direction of RS Oph. The scientific motivation for obtaining these data was to search for short period changes in line intensity, or velocity modulated effects (see Section 4.2.3).

The times of these observations in relation to the V-band light curve evolution<sup>1</sup> are shown in Fig. 1. Note the well-known dip in the light curve below the pre-eruption value around day 84, followed by eventual recovery by day 300. This is likely due to the blowing away of the accretion disc (AD) by

<sup>1</sup> Obtained from the AAVSO database <https://www.aavso.org/>

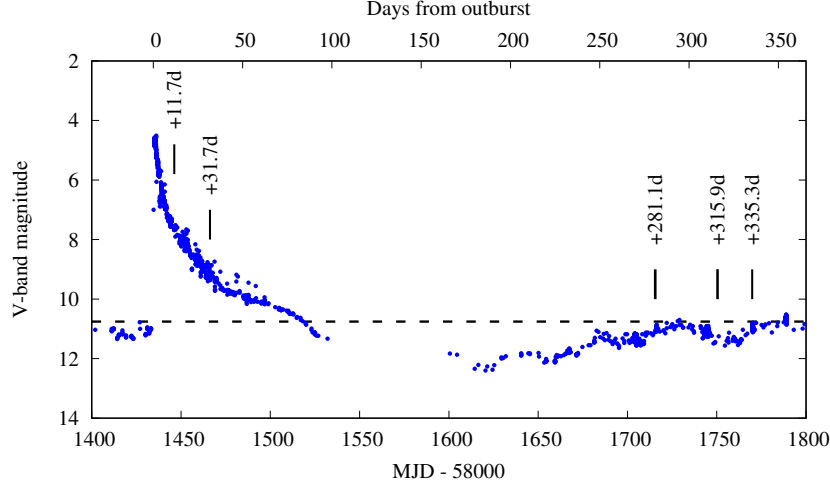


**Figure 1.** AAVSO  $V$  band light curve with the dates (see Table 1) of the IRTF spectroscopy marked (except for the days  $-428.1$  pre- and  $624.1$  post- outburst). In addition, spectra at high cadence were obtained on day 31.7 (see Section 4.2.3). The horizontal dotted line is the mean value of the pre-eruption (MJD  $< 591200$ )  $V$  magnitude.

the eruption, and its re-establishment by day 300 (see, e.g., Bode et al., 2006; Worters et al. 2007, for the resumption of accretion after  $\sim 200$  days following the 2006 eruption).

### 3.2 Swift

RS Oph was observed with the UV/Optical Telescope (UVOT) on the Neil Gehrels Swift Observatory (Gehrels et al. 2004). The data closest to our IRTF observations were obtained in the *uvm2* ( $2246\text{\AA}$ ) filter. The Swift photometry is given in Table 2; the UVOT magnitudes were converted to fluxes using the calibration given by Breeveld et al. (2011). The fluxes in Table 2 are not dereddened.

## 4 RESULTS

### 4.1 Quiescence: pre-eruption

A comprehensive optical ( $3900\text{--}7500\text{\AA}$ ) spectroscopic survey of RS Oph, with resolution up to 14000, was carried out by Habtie & Das (2025) over the period 2006–2021. Their data suggest that the emission lines in their spectra arose in the AD, and that a substantial change in the properties of the AD occurred in the lead-up to the 2021 eruption. They deduced an electron temperature for the AD of  $T_e \simeq 3.5 \times 10^4$  K, and an electron density  $N_e$  in the range  $\sim 3.8 \times 10^9$   $\text{cm}^{-3}$  to  $\sim 3.4 \times 10^{10}$   $\text{cm}^{-3}$ . They also deduced a temperature and luminosity for the central source, and a He abundance that is  $\sim$  twice solar during the earlier period of their study (2008–2014), decreasing to the solar value at later times (2018–2020). While the time-span of their data has little overlap with the data we present here, their study provides useful pointers for interpreting the NIR data.

Our first observation was obtained on 2020 June 10, 428.1 days before the 2021 eruption, and 5227.6 days ( $\sim 14.3$  years) after the 2006 eruption (which occurred on 2006

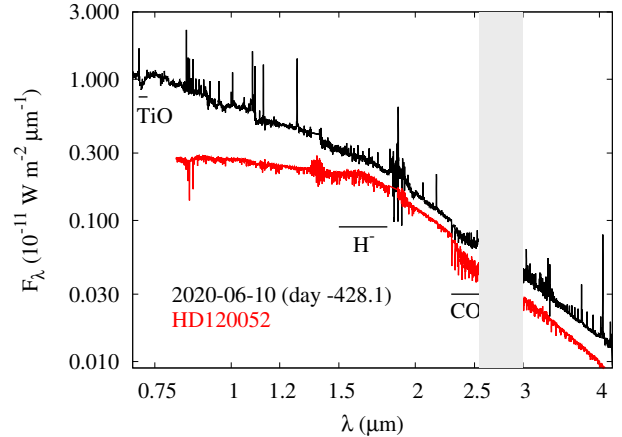


**Figure 2.** Quiescent (i.e., pre-2021 eruption) spectrum of RS Oph, obtained on 2020 June 10 (black). Grey block indicates wavelength region over which the atmospheric transmission is poor. Spectrum of the M2III star HD120052, scaled to that of RS Oph, is shown in red. Locations of the  $\gamma(0,0)$  TiO band (in RS Oph), the  $\text{H}^-$  continuum, and of the first overtone CO bands are indicated. (cf. Fig. 9).

February 12.83 UT, MJD 53778.83). We take the 2020 June observation to be close to “quiescence”, and subtract this spectrum from the two datasets obtained immediately after the 2021 eruption. This procedure is valid if we can be sure that there were no variations between the pre- and post-eruption observations. Note, however, that the 2020 June observation was obtained at the same orbital phase as the two post-eruption spectra, which should minimise the possibility of variability affecting the results.

The quiescent spectrum of RS Oph is shown in Fig. 2, together with that of the M2III field giant HD120052 from the IRTF Spectral Library (Cushing, Rayner & Vacca 2005;

**Table 1.** IRTF SpeX Observational Summary.

UT Date/Time	MJD <sup>a</sup> Days	$t - t_0$ (days) <sup>b</sup>	$\Phi^c$	SpeX Mode	Resolving power	SXD/LXD ITOT <sup>d</sup> (sec)
2020-06-10T09:37:05.663	59006.901	-428.1	0.783	SXD/LXD	1200	652/556
2021-08-20T04:52:18.456	59446.703	11.7	0.753	SXD/LXD	1200	178/574
2021-09-11T05:17:49.785	59466.721	31.7	0.797	SXD	1200	311/...
2022-05-16T13:24:50.957	59716.059	281.1	0.347	SXD/LXD	1200	593/566
2022-06-20T09:41:46.586	59750.904	315.9	0.424	SXD/LXD	1200	593/723
2022-07-10T08:15:43.383	59770.344	335.3	0.466	SXD	1200	949/...
2023-04-24T13:35:45.014	60058.566	624.1	0.103	SXD/LXD	750	297/834

<sup>a</sup>Julian Date -2 450 000.<sup>b</sup>Day 0  $\equiv t_0 = 59434.50$ , 2021 Aug 08.50 ( $\pm 0.01$ ).<sup>c</sup>Phase using ephemerides of [Brandt et al. \(2009\)](#).<sup>d</sup>Total integration time.**Table 2.** Swift UVOT photometry.

MJD Days	$t - t_0$ (days)	<i>uvm2</i> (2221Å)	Flux ( $10^{-14}$ W m <sup>-2</sup> $\mu$ m <sup>-1</sup> )	<i>uvw2</i> (1191Å)	Flux ( $10^{-14}$ W m <sup>-2</sup> $\mu$ m <sup>-1</sup> )
59466.36	31.86	< 10.42	> 314	< 10.95	> 222
59722.03	287.53	15.04 $\pm$ 0.03	4.49 $\pm$ 0.11	—	—
59750.44	315.94	14.54 $\pm$ 0.03	7.07 $\pm$ 0.17	—	—
59782.23	347.75	14.74 $\pm$ 0.03	5.92 $\pm$ 0.15	—	—

[Rayner, Cushing, & Vacca 2009](#)). It is apparent that the spectra of RS Oph and HD120052 are very similar longward of 1.8  $\mu$ m, although the first overtone CO bands seem somewhat weaker in RS Oph. However shortward of 1.8  $\mu$ m, there seem to be two distinct differences. First, the steep rise of the RS Oph spectrum to the blue; this is likely due to the presence of the AD. Second, the relative weakness in RS Oph of the H<sup>-</sup> continuum around 1.6  $\mu$ m. This is not surprising, given the low binding energy ( $\sim 0.75$  eV) of H<sup>-</sup>, and the harsh environment experienced by the RG photosphere. The quiescent observation was carried out when RS Oph was in quadrature (see Table 1).

There are three possible sources for the few emission lines present on day -428.1: the RG wind itself, the AD, and the material that bears the silicate grains seen in the aftermath of the 2006 eruption ([Evans et al. 2007c](#); [Woodward et al. 2008](#)). In each case it is likely that the emitting material is photo-ionised by the WD, and hard radiation from the inner AD. A list of the more prominent lines is given in Table A1. We have estimated the line fluxes by fitting one or more gaussians to the line profiles. The fluxes listed in Table A1 are for the strongest, central, component where the structure of the line is complex.

#### 4.1.1 The H recombination lines

The flux in the H recombination lines enables us to estimate the mass of emitting hydrogen if the lines selected are optically thin. For a uniform medium, we have

$$\frac{M_{\text{H}}}{M_{\odot}} = 8.98 \times 10^{17} D_{2.71}^2 \frac{f_n \lambda_n}{A_n n^2 b_n} \frac{T_e^{3/2}}{N_e} \exp \left[ -\frac{1.569 \times 10^5}{n^2 T_e (\text{K})} \right], \quad (2)$$

where  $N_e$  is in cm<sup>-3</sup> and  $D_{2.71} \equiv 1$  for RS Oph. In equation (2),  $f_n$  and  $\lambda_n$  are respectively the line flux (in W m<sup>-2</sup>)

and wavelength (in  $\mu$ m) of the line originating in upper level  $n$ , and  $A_n$  is the Einstein spontaneous emission coefficient. The coefficients  $b_n$  that describe departure from thermal equilibrium are taken to be

$$\begin{aligned} b_n &= 0.047 T_e^{0.25} \exp[-T_n/T_e] \\ &(5 \leq n \leq 10; \quad 5000 \leq T_e (\text{K}) \leq 3.2 \times 10^5) \\ &\equiv 1 \quad (T_e > 3.2 \times 10^5 (\text{K})) . \end{aligned} \quad (3)$$

The form of  $b_n$  for the lower  $T_e$  range has been obtained by fitting the  $T_e$ -dependence of the various  $b_n$  in [Baker & Menzel \(1938\)](#). The  $T_n$  values differ for different values of  $n$ ; for  $n = 8$  and 9, used here,  $T_8 = 5145$  K,  $T_9 = 4031$  K.

A simple test of optically thin-ness may be carried out on lines originating in the same upper level  $n$ , for example Bre (9-4) and Pfd (9-5). In such cases the flux ratios depend only on the wavelengths,  $\lambda_n$ , and Einstein emission coefficients  $A_n$  of the respective lines, which we take from [van Hoof \(2018\)](#)'s Atomic Line List (v3.00b5)<sup>2</sup>.

Table A1 shows that the flux ratio for these lines arising from  $n = 9$  is  $\sim 0.56$ , close to the expected value of 0.50 for optically thin emission. We use this line pair to estimate the mass of emitting H in the quiescent spectrum.

As noted above, there are three possible sites for the H emission lines: the RG wind, the AD, and the material that bears the silicate dust ([Evans et al. 2007c](#); [Woodward et al. 2008](#)) and we examine each case below:

(i) The RG wind. If the H lines are produced in the RG wind, we use an estimate of  $T_e \sim 8900$  K (see below). In this case  $M_{\text{H}}/M_{\odot} \simeq 950/N_e$ , with  $N_e$  in cm<sup>-3</sup>. From the mass-loss rate and the time interval  $\Delta t$  between the 2006 eruption and our 2020 observation ( $\simeq 5227$  days), the wind mass is  $\sim 1.4 \times 10^{-6} M_{\odot}$ , independent of the distance; this

<sup>2</sup> <https://linelist.pa.uky.edu/newpage/>

requires that  $N_e \simeq 6.6 \times 10^8 \text{ cm}^{-3}$ . The mass-loss rate from the RG implies an electron density at the Roche lobe radius of  $\sim 3.4 \times 10^9 \text{ cm}^{-3}$ . Given the approximations, this value of  $N_e$  seems consistent with the supposition that the H recombination lines arise in the RG wind.

(ii) The AD. The mass of the AD may be estimated from  $7 \times 10^{-10} [R_{\text{disc}}/3 \times 10^{10} \text{ cm}]^3 M_{\odot}$ , where  $R_{\text{disc}}$  is the outer disc radius (Wynn 2008). For a “cold” disc (see Wynn 2008, for details),  $R_{\text{disc}} \sim 10^{12} \text{ cm}$ , giving a disc mass of  $2.6 \times 10^{-5} M_{\odot}$ ; for a “hot” disc,  $R_{\text{disc}} \sim 10^{11} \text{ cm}$  and the disc mass is  $2.6 \times 10^{-8} M_{\odot}$ . Using the  $N_e$  and  $T_e$  values from Habtie & Das (2025), which apply to the AD, we find  $M_{\text{H}}$  in the range  $1.2 \times 10^{-7} M_{\odot}$  to  $1.2 \times 10^{-6} M_{\odot}$ . As this range excludes the estimates of the AD mass, an origin in the AD seems implausible, but with the caveat that we have implicitly assumed that the AD is optically thin.

However, an alternative estimate of  $T_e$  comes from the coronal lines [Si VI]  $\lambda = 1.965 \mu\text{m}$  and [Si IX]  $\lambda = 3.9357 \mu\text{m}$ , both of which are present in the 2020 spectrum (see Table A1 for data, and Section 4.2.1.2 below for methodology). The flux ratio in these lines implies  $T_e \simeq 5.5 \times 10^5 \text{ K}$ , substantially higher than the value found ( $3.5 \times 10^4 \text{ K}$ ) by Habtie & Das (2025). The discrepancy is likely due to the fact that their (optical) study did not include any coronal lines, the presence of which inevitably inflates the temperature estimate. This value of  $T_e$  gives  $M_{\text{H}}/M_{\odot} \simeq 1.5 \times 10^5/N_e$ , with  $N_e$  in  $\text{cm}^{-3}$ . The critical electron density for both these Si lines, above which the upper level is collisionally de-excited, is  $\sim 10^9 \text{ cm}^{-3}$  at  $5.5 \times 10^5 \text{ K}$ . As this implies that  $N_e \lesssim 10^9 \text{ cm}^{-3}$ , this leads to  $M_{\text{H}} \gtrsim 1.5 \times 10^{-4} M_{\odot}$ , considerably higher than the estimates of the AD mass. We conclude that the H recombination lines cannot arise in the AD.

(iii) Woodward et al. (2008) estimated the mass of silicate dust seen in the Spitzer IRS data to be a model-dependent  $\sim 2 \times 10^{-9} M_{\odot}$ . For a reasonable dust-to-gas ratio ( $\sim 0.01$ ), the total mass of this material would be  $\sim 2 \times 10^{-7} M_{\odot}$ . If we take the same parameters as for the RG wind, then  $M_{\text{H}}/M_{\odot} \simeq 950/N_e$ . In addition to the silicate features, the Spitzer IRS data show the presence of the [Ne II]  $12.81 \mu\text{m}$  and [O IV]  $25.91 \mu\text{m}$  fine structure lines (Rushon et al. 2022). The critical densities for these lines at  $10^4 \text{ K}$  are  $7.03 \times 10^5 \text{ cm}^{-3}$  (Gehrz et al. 2008) and  $9.94 \times 10^3 \text{ cm}^{-3}$  (Helton et al. 2012) respectively. As these are upper limits on  $N_e$ , the implied  $M_{\text{H}} \gtrsim 1.4 \times 10^{-3}$ , ruling out this interpretation.

The H mass as inferred from the H recombination lines therefore point to an origin in the RG wind, ionised by hard radiation from the WD and inner AD.

There is evidence for neither a Paschen nor a Brackett discontinuity in the spectrum. The contribution of any free-free and free-bound emission for the case of a pure hydrogen plasma may be set by the H line fluxes using the NEBCONT task in the STARLINK (Currie et al. 2014; Bell et al. 2024) package. Using the Pf $\delta$  line flux to set the level of the free-free and free-bound emission leads to a continuum that is  $\gtrsim 10$  times lower than that observed at the shortest wavelengths.

#### 4.1.2 Metal lines

Also present in the quiescent spectrum are O I fluorescent lines and the calcium triplet.

The O I lines at  $0.8446 \mu\text{m}$  and  $1.1288 \mu\text{m}$  are produced

by the Bowen (1947) fluorescence mechanism. Each transition giving rise to a  $1.1288 \mu\text{m}$  photon leads to the emission of an  $0.8446 \mu\text{m}$  photon (Rudy et al. 2003). This is essentially borne out by the respective photon fluxes in Table A1,  $\sim 4.0 \times 10^4 \text{ photons m}^{-2} \text{ s}^{-1}$  ( $1.1288 \mu\text{m}$ ) and  $\sim 4.3 \times 10^4 \text{ photons m}^{-2} \text{ s}^{-1}$  ( $0.8446 \mu\text{m}$ ). In their study of mass transfer in T CrB, Planquart, Jorissen & Van Winckel (2025) concluded that these O I lines arise in the “bright spot”, where the inter-star stream impacts the outer edge of the AD. Given the broad similarity between the RS Oph and T CrB systems, this seems a likely interpretation of the O I lines in the quiescent spectrum of RS Oph.

Also present in emission is the Ca II triplet at  $0.8500 \mu\text{m}$ ,  $0.8544 \mu\text{m}$ ,  $0.8664 \mu\text{m}$ . Allowing for the contribution of the Pa 11-3, 12-3, 14-3 lines to the Ca triplet (note that the flux values in Table A1 include contributions from both Ca II and Pa lines), the line Ca II fluxes are in the ratio 1:0.8:1.0, close to the ratio 1:1:1 for the case that the lines are optically thick; in the optically thin case the flux ratios would be 1:9:5 (Herbig & Soderblom 1980). These lines have been detected in a number of cataclysmic binaries by Persson (1988), who concluded that they most likely arise in the AD. Given that the Ca II triplet in the case of RS Oph appears to be optically thick, they likely arise, like the O I lines, in either the bright spot or the AD.

## 4.2 The 2021 eruption

The post-eruption spectra are shown in Fig. 3. The top and bottom panels cover the wavelength ranges  $0.7\text{--}2.5 \mu\text{m}$  and  $2.7\text{--}4.3 \mu\text{m}$ , corresponding to the SpeX Short-Cross Dispersed (SXD) and Long-Cross Dispersed (LXD) wavelength ranges, respectively. The central panel identifies a number of the stronger lines on day 31.7.

The NIR spectra in the immediate aftermath of the 2021 eruption are shown in Fig. 4, together with BVR photometry from the AAVSO database. The AAVSO data were obtained within hours of our NIR spectra; the photometric uncertainties as reported in the AAVSO data are typically  $\pm 0.02 \text{ mag}$  (and are thus smaller than the plotted points in Fig. 4).

The Paschen ( $0.821 \mu\text{m}$ ) and Brackett ( $1.459 \mu\text{m}$ ) discontinuities are clearly visible in both day 11.7 and day 31.7 spectra. Their magnitudes are suggestive of a relatively cool gas, and Evans et al. (2007a) suggested that the material responsible is the RG wind, ionised by the ultraviolet (UV) flash from the eruption (see also Shore et al. 1996). We explore this in more detail here by defining the “step height” (SH) of the Paschen and Brackett discontinuities as

$$\frac{f_{\lambda}(\lambda \rightarrow 0.821^{-} \mu\text{m})}{f_{\lambda}(\lambda \rightarrow 0.821^{+} \mu\text{m})} \quad \text{and} \quad \frac{f_{\lambda}(\lambda \rightarrow 1.459^{-} \mu\text{m})}{f_{\lambda}(\lambda \rightarrow 1.459^{+} \mu\text{m})} \quad (4)$$

respectively. The dependence of these quantities on electron temperature for a pure hydrogen plasma is shown in Fig. 5. The magnitudes of the discontinuities in RS Oph were determined by fitting the continuum blue-ward and red-ward of the discontinuity with a quadratic function, after removing the emission lines. We find SH(Pa)  $\simeq 2.56$ , SH(Br)  $\simeq 1.57$  (day 11.7), and SH(Pa)  $\simeq 3.81$ , SH(Br)  $\simeq 1.68$  (day 31.7). There is no evidence that the electron temperature changed between days 11.7 and 31.7, and in the following we adopt a mean  $T_e = 8900 \pm 300 \text{ K}$ .

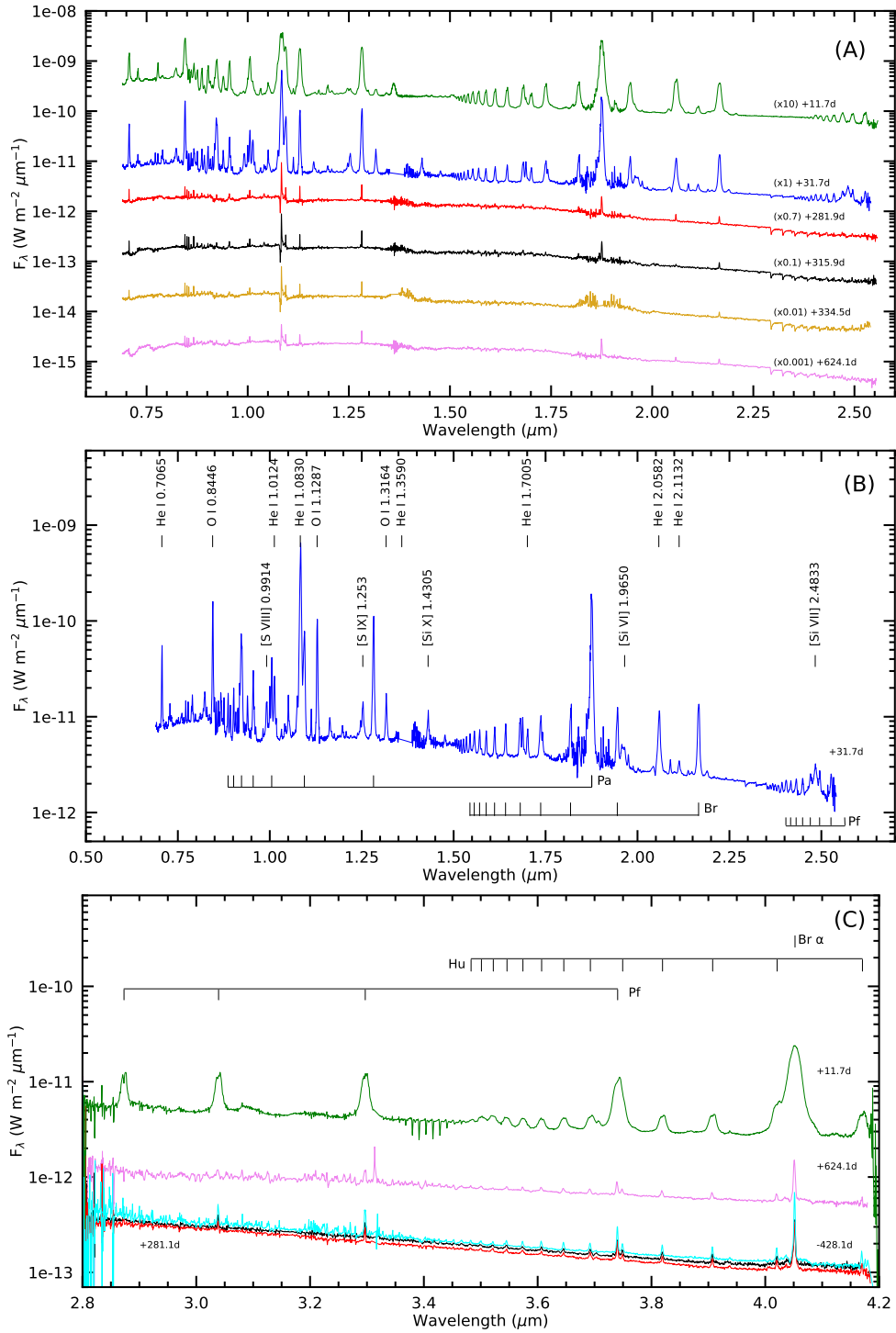


**Figure 3.** Observed near-infrared spectra of RS Oph at different epochs (Table 1). (A): Evolution of the SpeX SXD 0.7–2.5  $\mu\text{m}$  range; data are offset by values stated in the figure for clarity. (B) SpeX SXD 0.7–2.5  $\mu\text{m}$  spectra obtained on day +31.7. Indicated in the panel are the wavelength of various hydrogen emission line series (Brackett, Paschen, Pfund). Representative He and O lines are also identified, together with various infrared coronal lines. (C): Evolution of SpeX LX mode (thermal wavelengths) 2.7–4.3  $\mu\text{m}$  range. Days past outburst are indicated, together with the wavelengths of emission lines in the hydrogen Brackett, Humphries, and Pfund series. The absorption features around 3.4  $\mu\text{m}$  on day +11.7 are telluric.

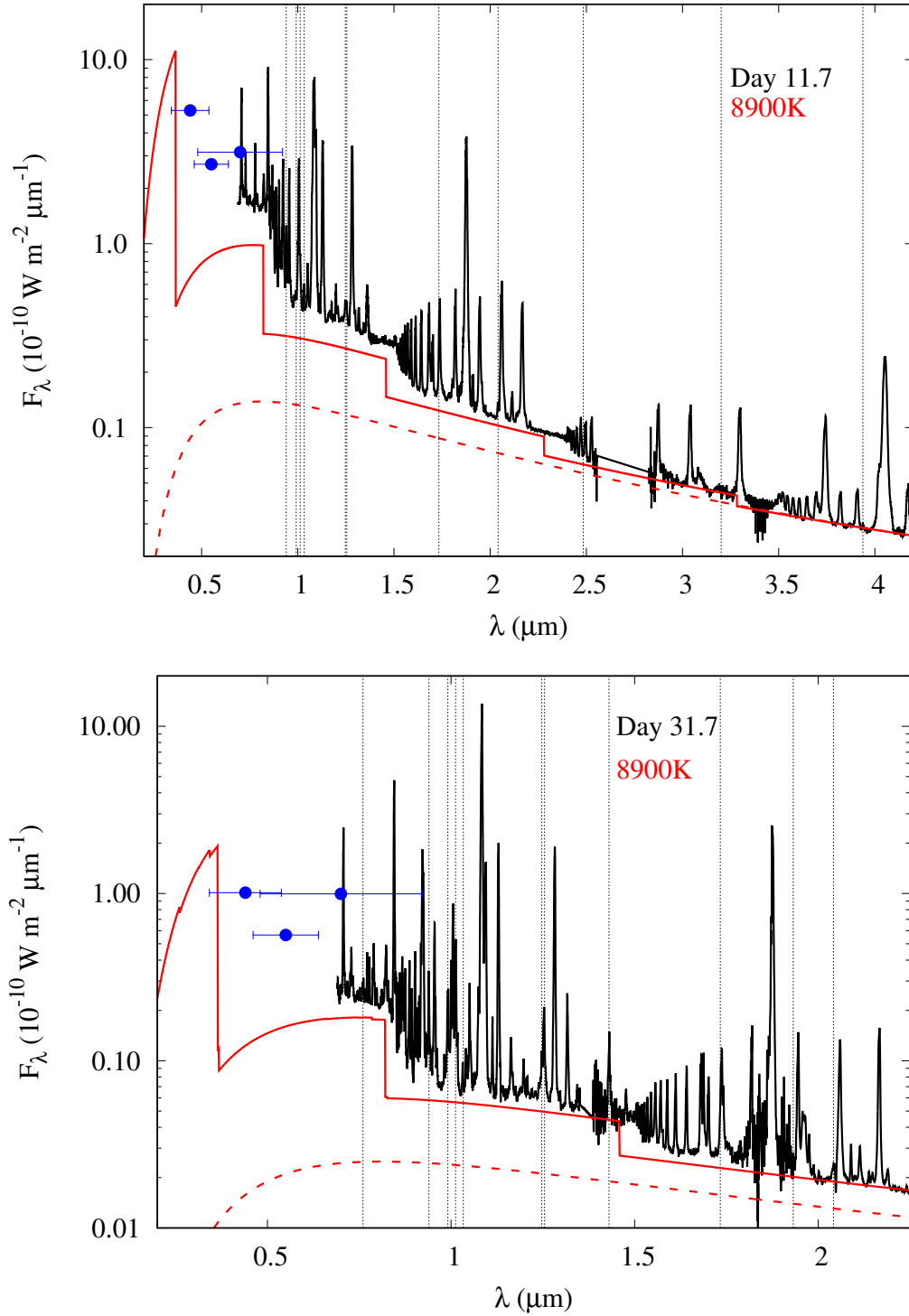


**Figure 4.** Top: IRTF spectrum for day 11.7; bottom: spectrum for day 31.7. Coronal lines are indicated by the vertical dotted lines (see Table A1). Data are shown in black. Full red curves are nebular continua for temperature 8900 K, for which the scale is set by H line fluxes. Broken line in top frame is the free-free continuum for temperature 8900 K, for which the scale is set by fitting the long ( $\lambda > 3.6 \mu\text{m}$ ) wavelength continuum. Broken line in bottom frame is the 8900 K free-free day 31.7 data as described in text. Blue points are AAVSO *BVR* data, for which the wavelength “error bars” are the FWHM of the *BVR* filters. See text for details. The plots are extended to  $0.3 \mu\text{m}$  to show the expected extent of the Balmer discontinuity.

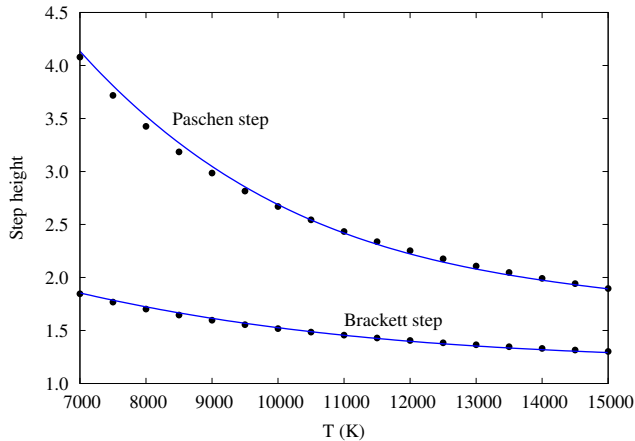


**Figure 5.** Dependence of the Paschen and Brackett discontinuities on temperature for a pure hydrogen plasma. Black points: theoretical values from [Baker & Menzel \(1938\)](#); blue lines are polynomial fits.

#### 4.2.1 Day 11.7

The day 11.7 spectrum is shown in Fig. 4 (top panel), together with AAVSO *BVR* data. At this time, the spectrum was dominated by H and He emission lines, including Br 19-4  $\rightarrow$  5-4, Hu 24-6  $\rightarrow$  13-6, Pf 23-5  $\rightarrow$  8-5 series, and some of the Paschen series. Lines of carbon (e.g., C I 1.175  $\mu\text{m}$ ), nitrogen (e.g., N I 1.247  $\mu\text{m}$ ), and oxygen (e.g., O I 0.8446, 1.129, and 1.3171  $\mu\text{m}$ ) were present, as is the Ca II triplet at  $\approx 0.86 \mu\text{m}$ . The photon fluxes in the Bowen-fluoresced O I lines are again comparable,  $\sim 1.7 \times 10^7 \text{ m}^{-2} \text{ s}^{-1}$  (0.8446  $\mu\text{m}$ ) and  $\sim 1.3 \times 10^7 \text{ m}^{-2} \text{ s}^{-1}$  (1.1288  $\mu\text{m}$ ). The fluxes of the Ca triplet are in the ratio 1.0:0.8:2.3, somewhat different from the ratios expected for the optically thick case (see Section 4.1).

The H lines consisted of a main peak, with wings to the blue and red. The FWHM of the main peaks of the H lines, corrected for spectral resolution, correspond to a mean expansion velocity of  $\approx 680 \text{ km s}^{-1}$ . The wings were displaced by  $\sim -1200 \text{ km s}^{-1}$  and  $\sim +1900 \text{ km s}^{-1}$ , with the fluxes in the blue wings being  $\sim 4$  larger than those in the red (see Fig 6). A likely interpretation is that the main peaks arise in a torus-like structure, while the wings arise in outflows perpendicular to the torus. Taking the orbital inclination into account, and assuming that the torus lies in the orbital plane, the outflow velocities are  $\approx -650 \text{ km s}^{-1}$  and  $\approx +2200 \text{ km s}^{-1}$ .

**4.2.1.1 Hydrogen emission:** For the purpose of the present paper, we have computed the 8900 K nebular continuum (as implied by the NIR discontinuities; see above) for a plasma consisting of H and 10% He by number ([Habtie & Das 2025](#)). A more thorough treatment of the continuum and line emission will be given in a future paper. In the NEBCONT task, the scale of the nebular continuum is determined by the  $\text{H}\beta$  flux, which is not available. We therefore use the flux in the central component of the  $\text{Br}\alpha$  flux for day 11.7, and the assumption of “Case B”, to estimate the  $\text{H}\beta$  flux. This procedure does of course assume that the H recombination lines and the 8900 K nebular continuum arise in the same region, and that Case B applies, but we allow for this by scaling the continuum by a factor  $\lesssim 5$ . The result is shown

in Fig. 4 (top panel), together with the dereddened AAVSO *BVR* data. In addition to the Paschen and Brackett discontinuities, the Pfund (2.279  $\mu\text{m}$ ) and Humphries (3.282  $\mu\text{m}$ ) discontinuities are also evident. Our simple model satisfactorily reproduces the size of the NIR discontinuities. However, we draw attention to the expected large Balmer discontinuity, which was not present in an optical spectrum obtained by [Munari & Valisa \(2021\)](#) within four hours of our day 11.7 observation.

There may also be some evidence for an increasing discrepancy between the data and the 8900 K nebular continuum as we go to shorter wavelengths. The AD, which was not re-established until after day 225 ([Munari & Tabacco 2022](#)), can surely make no contribution at this early time. A possible candidate is bremsstrahlung emission from the hot coronal gas, but no combination of 8900 K gas and  $10^{6.0}$  K gas (see Section 4.2.1.2 below) can account for the discrepancy. A similar shortfall was present in the day 11.81 spectrum of the 2006 eruption (see Figure 4 of [Evans et al. 2007a](#)). These factors almost certainly highlight the complexity of the RS Oph environment compared with the simplicity of the model. A more sophisticated approach will be presented in a future paper.

Notwithstanding the above caveats, we use the free-free emission to estimate the mass of emitting H (note that the use of the H recombination lines for this purpose, as was done in Section 4.1, is complicated for spectra during eruption by the overlap of several H I and He II lines and possible “contamination” by lines from the still-undisturbed RG wind). The free-free flux  $f_{\text{ff}}$  per unit wavelength interval is (e.g., [Cox 2000](#))

$$f_{\text{ff}} = \frac{32\pi e^6}{3m^2 c^3} \left( \frac{2\pi m c^2}{3kT} \right)^{1/2} \frac{N_e(\text{cm}^{-3})}{4\pi D^2} \frac{1}{m_p} \left( \frac{M_{\text{H}}}{M_{\odot}} \right) \times \bar{g}_{\text{ff}} \lambda^{-2} \exp\left(-\frac{hc}{\lambda k T_e}\right). \quad (5)$$

(in cgs units), and  $\bar{g}_{\text{ff}}$  is the temperature-averaged gaunt factor. The latter is virtually independent of wavelength over the range 3.6–4.2  $\mu\text{m}$ , where it has a value of 1.1 ([Karzas & Latter 1961](#)); we take  $T_e = 8900 \text{ K}$ . Fitting the data longward of the Humphries discontinuity (thus avoiding the larger discontinuities at shorter wavelengths) gives

$$\frac{M_{\text{H}}}{M_{\odot}} \approx \frac{207}{N_e(\text{cm}^{-3})} \quad (6)$$

for a distance of 2.71 kpc. This free-free continuum is shown by the broken curve in Fig. 4. By day 11.7, the shocked ejecta will have reached a distance

$$r_{\text{shock}} = \frac{3}{2} V_0 t_0 [t/t_0]^{2/3}, \quad (7)$$

(appropriate for “Phase II” of its evolution; see [Bode & Kahn 1985](#), for details) from the site of the explosion; here  $V_0$  is the ejecta velocity at an early time  $t_0$ . [Taguchi et al. \(2021\)](#) found  $V_0 = 2600 \text{ km s}^{-1}$  one day after the eruption, so the shock radius is  $r_{\text{shock}} \approx 3.4 \times 10^{11} [t/\text{days}]^{2/3} \text{ m} \approx 1.7 \times 10^{12} \text{ m}$  on day 11.7. Note that the shock would reach the outer edge of the wind, “breakout”, at  $t = 138$  days in this case. The outer radius of the undisturbed wind at this time is  $\approx 8.1 \times 10^{12} \text{ m}$ , so that the mass of undisturbed (i.e., cool) wind is  $\sim 1.3 \times 10^{-6} M_{\odot}$ . This implies  $N_e \sim 1.6 \times 10^8 \text{ cm}^{-3}$ , but we should be mindful of the fact that the wind is unlikely to be uniform.

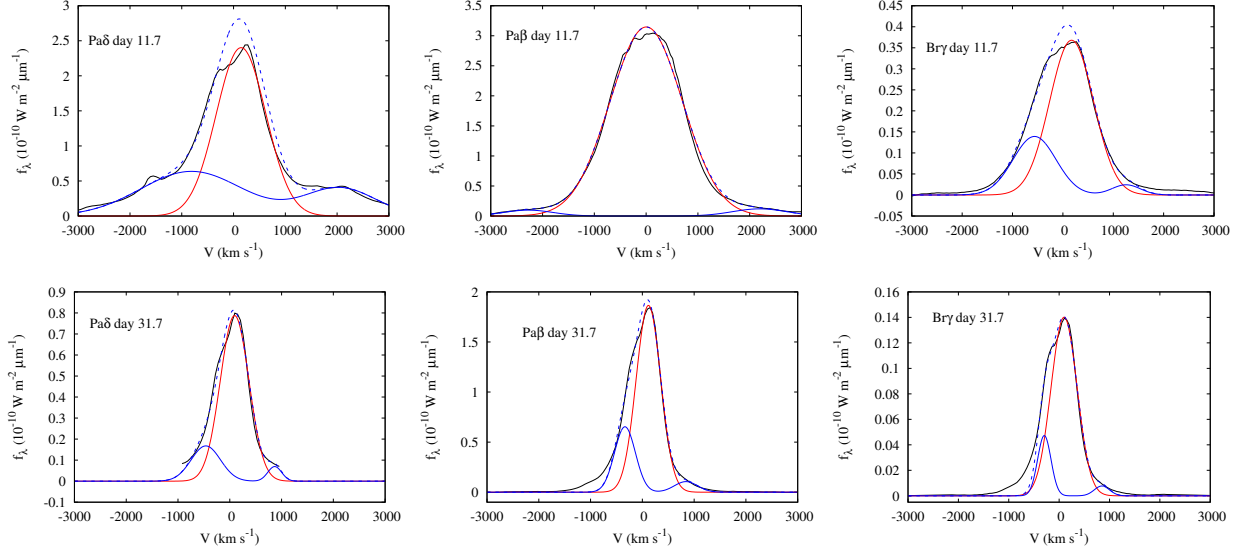


**Figure 6.** Sample of H recombination lines profiles. Black lines: continuum-subtracted data. Red lines: gaussian fit to line core. Blue lines: gaussian fits to line wings. Blue dashed lines: sum of core and wing fits. See text for details.

**4.2.1.2 Coronal lines:** There are several coronal lines in the day 11.7 spectrum. We use these, as in previous work (e.g., Woodward et al. 2021; Evans et al. 2022), to estimate the temperature  $T_{\text{cor}}$  of the coronal gas; we defer the determination of abundances to a future paper. In general, the coronal lines (unlike the H recombination lines) are unresolved, and so presumably arise in the same region of the ejecta so that the  $T_{\text{cor}}$  may be averaged. The ratio of the line fluxes for a pair  $a$  and  $b$  of ionisation states of the same element is

$$\frac{f_a}{f_b} = \frac{n_a}{n_b} \frac{\lambda_b}{\lambda_a} \frac{\Upsilon_a(T_{\text{cor}})}{\Upsilon_b(T_{\text{cor}})} \frac{\omega_b}{\omega_a} \quad (8)$$

(Greenhouse et al. 1990), where the  $f$  values are the measured line fluxes, the ratio  $n_a/n_b$  is a function of  $T_{\text{cor}}$ , and the  $\omega$  values are the statistical weights of the lower levels.

We use effective collision strengths from the IRON project<sup>3</sup> (Hummer et al. 1993; Badnell et al. 2006). This dataset gives  $\Upsilon$ , the effective collision strengths, averaged over a Maxwell speed distribution, over a wide range of temperatures; where the  $\Upsilon$  values do not go above temperature  $10^5$  K, we use the value at  $10^5$  K. Ionisation fractions as a function of temperature are determined using the data in Arnaud & Rothenflug (1985). Using the ion pairs listed in Table 3, we find a mean value  $\log T_{\text{cor}} = 5.99 \pm 0.07$ , or  $T_{\text{cor}} = 10^{6.0 \pm 0.1}$  K, for day 11.7.

#### 4.2.2 Day 31.7

The day 31.7 spectrum is shown in Fig. 4 (bottom panel), together with dereddened  $BVR$  photometry from the AAVSO database. The H lines again consisted of a main peak, with wings to the blue and red (see Fig. 6). However, there was a significant change in that (a) the velocity of the material from which the wings arise has decreased significantly, from  $-1200 \text{ km s}^{-1}$  to  $-440 \text{ km s}^{-1}$ , and from  $+1900 \text{ km s}^{-1}$

**Table 3.** Coronal lines used to estimate temperature of coronal gas. See text for details.

Day	Line pair	$\log T_{\text{cor}}$ (K)
11.7	[S XII]–[S IX]	6.13
	[S VIII]–[S IX]	5.76
	[S IX]–[S VI]	> 6.5
	[Si VII]–[Si IX]	5.92
	[Al VIII]–[Al IX]	6.15
31.7	[Si VI]–[Si X]	5.89
	[Si VII]–[Si X]	5.89

to  $+850 \text{ km s}^{-1}$ , and (b) the line widths had also decreased substantially. This deceleration is a consequence of the encounter of the ejecta with the RG wind, and was first quantified for the case of RS Oph by Bode & Kahn (1985), who showed that the outer shock radius at time  $t$  is  $r_{\text{shock}} \propto t^{2/3}$  ( $V \propto t^{-1/3}$ ) during Phase II of the development of the remnant.

As for the day 11.7 data, the 8900 K nebular continuum, scaled by the  $\text{Br}\gamma$  flux, is included. It is evident in Fig. 4 that, as on day 11.7, the predicted nebular continuum falls short of matching the spectrum at the shortest wavelengths, suggesting another source of continuum radiation.

The spectrum is again dominated by H recombination and coronal lines. The Bowen O I lines have photon fluxes  $4.2 \times 10^6 \text{ m}^{-2} \text{ s}^{-1}$  ( $0.8446 \mu\text{m}$ ) and  $3.2 \times 10^6 \text{ m}^{-2} \text{ s}^{-1}$  ( $1.129 \mu\text{m}$ ), while the flux ratios of the Ca II triplet are 1.0:0.5:0.2.

The  $^{12}\text{C}^{16}\text{O}$  band heads from  $2.29 \mu\text{m}$  onwards, arising from the RG secondary, were clearly detected. This is much earlier than in the 2006 outburst, when they were not visible 55 days after the 2006 eruption (Evans et al. 2007a), although the cadence of the NIR spectroscopy was different for the 2006 and 2021 eruptions. The CO bandheads are quite distinct  $\gtrsim 280$  days after the outburst as the system returns to

<sup>3</sup> <http://cdsweb.u-strasbg.fr/tipbase/home.html>

quiescence (see Fig. 7). The CO bands are further discussed in Section 4.4.2.

**4.2.2.1 Coronal lines:** IR coronal lines of [S VIII] 0.9914  $\mu\text{m}$  (ionisation potential of the lower ionisation stage 281 eV), [S IX] 1.253  $\mu\text{m}$  (329 eV), [Si X] 1.403  $\mu\text{m}$  (351 eV), [Si VII] 1.9650  $\mu\text{m}$  (167 eV), and [Si VII] 2.4833  $\mu\text{m}$  (205 eV) appeared, just after the onset of the SSS on day 20.6 (Page et al. 2022). There are no data longward of 2.5  $\mu\text{m}$ , and we estimate the temperature of the coronal gas using the Si lines [Si X] 1.403  $\mu\text{m}$ , [Si VII] 1.9650  $\mu\text{m}$ , and [Si VII] 2.4833  $\mu\text{m}$ . We find that  $T_{\text{cor}} = 10^{5.9}$  K, not significantly different from that on day 11.7.

**4.2.2.2 Hydrogen emission:** The 8900 K continuum still provides a reasonable description of the shape of the NIR continuum. However in the absence of LXD data we can not, as we did for the day 11.7 spectrum, fit a pure free-free continuum to the data using equation (5). However we scale the fit to day 11.7 by matching the free-free flux at 2  $\mu\text{m}$  to the nebular continuum. The match is good if the day 11.7 free-free continuum is scaled by a factor 0.18; this continuum (again for 8900 K) is shown in the bottom panel of Fig. 4. The implied mass of hydrogen is  $M_{\text{H}}/M_{\odot} \simeq 37/N_e$ . By day 31.7, the outer edge of the undisturbed wind is at  $8.85 \times 10^{12}$  m, whereas the shock is at  $3.38 \times 10^{12}$  m; the mass of the undisturbed wind is  $\sim 9.6 \times 10^{-7} M_{\odot}$ .

The change in the estimated H mass from the free-free emission by the cool gas likely rules out an origin in the silicate-bearing material, of mass  $\sim 2 \times 10^{-7} M_{\odot}$  (see Section 4.1). It is likely that this material is unaffected by the violent events occurring in the vicinity of the nearby binary. By day 31.7, the FWHM of the H emission lines had narrowed (velocities of  $610 \text{ km s}^{-1}$ ), and the red-wing asymmetries and saddle-shaped line profile peaks had disappeared.

#### 4.2.3 The high cadence observations

The continuum around, and the profile and width of, the He I line show no significant evidence of variability during this time, as may be seen in the top panel of Fig. 8. Note that the variations in the peak flux in the line are within the expected 10% uncertainty in the flux calibration (see Section 3.1). To further explore possible variation in the He I line on short time-scales, we extracted from the forty spectra obtained with the  $\sim 6$  s cadence a region of interest (ROI) from 1.0620  $\mu\text{m}$  to 1.1100  $\mu\text{m}$ , computed the local continuum from a first-order polynomial (python `np.polyfit(wavelength, flux, 1)`), using continua from 1.0620  $\mu\text{m}$  to 1.0680  $\mu\text{m}$ , and from 1.1020  $\mu\text{m}$  to 1.1100  $\mu\text{m}$ , creating continuum-normalised spectra over the ROI (Fig. 8, middle panel). A three-dimensional representation of these data is presented in Fig. 8, bottom panel). There is no clear evidence of marked variation in the He I 1.0830  $\mu\text{m}$  line over this period of  $\sim 240$  s. In particular, there is no evidence for any periodic variation (which might correspond, for example, to the 35 s QPOs seen in the X-ray data; Page et al. 2022).

However, deeper synoptic observations, at higher cadence, during the SSS phase of the next eruption are required to confirm this result. In particular, we plan similar high cadence spectroscopy during the imminent eruption of the SyRN

T CrB (Schaefer 2023, but see Merc et al. (2025) for a cautionary note).

### 4.3 Quiescence: post-eruption

It is of interest to compare the pre-2021 eruption spectrum with those obtained after the eruption had subsided. Fig. 9 shows the pre-eruption spectrum (day -428.1), along with the spectra obtained on days 335.3 and 624.1 after the 2021 outburst. In both of the later spectra, the post-eruption continuum lies below the pre-eruption spectrum, particularly in the blue on day 624.1; recall that the latter was obtained when the RG was at inferior conjunction, so the visible hemisphere of the RG would not have been affected by the WD.

In the post-eruption spectra, the He I line at 1.0833  $\mu\text{m}$  shows a prominent P Cygni profile, with terminal velocity  $\sim -1500 \text{ km s}^{-1}$ . The He I line at 0.7067  $\mu\text{m}$  is clearly present on day 335.3. On day 624.1, it is weakly present; it too seems to have a P Cygni profile, with terminal velocity  $\sim 1000 \text{ km s}^{-1}$ , but its presence close to the TiO band head makes drawing any quantitative conclusion difficult. The H recombination lines show no such structure. The presence of P Cygni profiles in the He I lines, but not H I, suggests that, at this time, the He is located in a wind that still emanates from the WD, whereas the H may be located in the “permanent” circumstellar material associated with the RS Oph system.

The Ca II triplet, which was present in the pre-eruption spectrum (see Fig. 2), is also present in the quiescent post-eruption spectra, as are the Bowen-fluoresced O I lines.

There are simultaneous data (Swift UVOT, AAVSO BVRI, IRTF) for Day 315.9. As in Fig. 2, we compare the spectral energy distribution (SED) of RS Oph with that of HD120052 (Fig. 10). There is an offset ( $\sim 60\%$ ) between the photometry and the spectroscopy, likely due to the uncertainty in the flux calibration of the NIR spectrum. However it is again evident that, as in the pre-eruption quiescent spectrum (Fig. 2), there is a large discrepancy between the SED and that of the field giant in the blue-UV. We again attribute this to the presence of the AD, which will have been re-established by day 315.9, and likely as early as day 225 (Munari & Tabacco 2022).

### 4.4 The molecular bands

#### 4.4.1 The TiO and CN bands

The three TiO bands at 0.705  $\mu\text{m}$  ( $\gamma(0,0)$ ), 0.759  $\mu\text{m}$  ( $\gamma(0,1)$ ), and 0.843  $\mu\text{m}$  ( $\epsilon$ ) are present pre- and post-eruption, but their prominence in each case differs considerably (see Fig. 9). The 0.705  $\mu\text{m}$  band is formed in the outer layers of the RG photosphere, the 0.759  $\mu\text{m}$  band at somewhat deeper layers, and the 0.843  $\mu\text{m}$  band at even deeper layers.

Only the 0.705  $\mu\text{m}$  band is present on day -428.1 (Fig. 2), and possibly on day 335.3. However it is evident that these three TiO bands are present on the last (day 624.1) spectrum. In the spectra of S-type symbiotic stars described by Mürset & Schmid (1999), all three bands are present in a M7.5 RG, but only the 0.705  $\mu\text{m}$  band in earlier (M0, M3.5) RGs. While irradiation of the RG by either the WD or the AD has negligible effect on the effective temperature of the RG, the TiO bands in RS Oph may suggest a change in the effective spectral type of the RG secondary, before and after

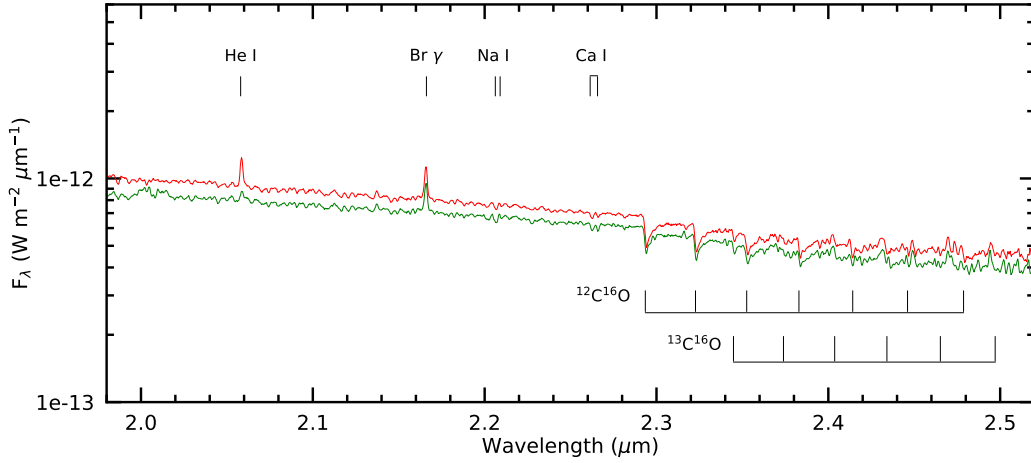


**Figure 7.** The CO bandheads from the giant secondary as they emerge again to dominate the absorption features longward of  $2.3 \mu\text{m}$  late in the post-outburst (2021) evolution of RS Oph. Red: spectrum from 2022 May 16; green: spectrum from 2022 June 20.

the eruption. Indeed, in Fig. 9, it may be seen that the overall slope of the SED for day 624.1 suggests a lower effective temperature.

We do not consider that the changes in the TiO bands are related to the 2021 outburst. Pavlenko et al. (2016) presented six optical spectra, the first of which was obtained 7 months after the 2006 outburst. All of these spectra, including the first, have deep TiO bands, in particular the  $\gamma'$  band (band head at  $0.620 \mu\text{m}$ ). This suggests that the 2006 outburst did not affect the TiO bands, and we can expect that this was also the case in 2021. There is no significant variability in the TiO bands among the spectra shown by Pavlenko et al. (2016), but all those spectra were obtained when the binary was approximately in quadrature. In the present data, the day  $-428$  spectrum (Fig. 2) was also obtained close to quadrature, and the  $\gamma(0,0)$  band is relatively strong. On days 281, 315 and 335, when the binary was also in quadrature, the spectra show weak TiO bands, especially on day 335.3 (phase 0.466), when the bands are weakest. On day 624.1, the RG was at inferior conjunction, and there would have been no effect of the WD and AD; as expected, this is when the TiO bands are strongest.

We considered the possibility that the TiO bands might partially be formed in the shell, but we regard this as unlikely. If this were the case, the presence of the shell would also be apparent in the CO first overtone bands. However, our modeling of the high resolution spectra of RS Oph in Pavlenko et al. (2010) showed that the CO bands are reproduced quite well using a single model atmosphere, without additional layers.

There are a number of possible sources of radiation in the environment of the RG (e.g., the WD, the boundary layer, the RG wind and still-present ejecta) which might result in the “dilution” of the TiO bands. A detailed consideration of this issue is complex, and beyond the scope of this paper.

Also detected are the CN bands  $\Delta v = 0 R_2$  (band head at  $1.0932 \mu\text{m}$ ),  $R_1$  ( $1.0971 \mu\text{m}$ ) and  $Q_1$  ( $1.1004 \mu\text{m}$ ); these are indicated on the bottom panels of Fig. 9. These bands are commonly seen in the spectra of field RGs, and we therefore conclude that they originate in the RG component of RS Oph.

Weak  $3 \mu\text{m}$  H<sub>2</sub>O lines are also present on day 624, when the RG effective temperature was lowest; they may also be present on day  $-428$ .

#### 4.4.2 The first overtone CO bands

The  $^{12}\text{C}^{16}\text{O}$  band heads from  $2.29 \mu\text{m}$  onwards, arising from the RG, were present in the day 31.7 spectrum (see Section 4.2.2). They were not present 55 days after the 2006 eruption (Evans et al. 2007a), and were first detected on day 170 (Rushton et al. 2010). This behaviour during the 2021 eruption is similar to that of the SyRN V3890 Sgr (which also has a RG secondary), in which the CO bands were clearly present 31.35 days after its 2019 eruption (Evans et al. 2022). In RS Oph, the CO band heads are present on day 281.1 after the 2021 outburst, as the system returns to quiescence (see Figure 7).

#### 4.4.3 The first overtone SiO bands

There is some evidence for the presence of the  $^{28}\text{Si}^{16}\text{O}$  first overtone band heads at  $\sim 4 \mu\text{m}$ , both on day  $-428.1$  (before the 2021 eruption) and on day 624.1 (post-2021 eruption; see Fig. 11); there is no evidence for the presence of SiO in any other spectra. If present, they seem to be much weaker than they were in T CrB in 2019 (Pavlenko et al. 2020), seven decades after its 1946 eruption. However the signal-to-noise in the 2021 data is such that Si isotopic ratios can not be determined. However, high resolution IR spectra in the  $4 \mu\text{m}$  range should help determine isotopic ratios, as was done for T CrB (Pavlenko et al. 2020).

## 5 CONCLUSIONS

We have presented NIR spectra of RS Oph, immediately before, during, and after its 2021 eruption. Our conclusions are as follows:

- (i) emission lines observed prior to the eruption most likely arise in the red giant wind, illuminated by the white dwarf and the accretion disc;

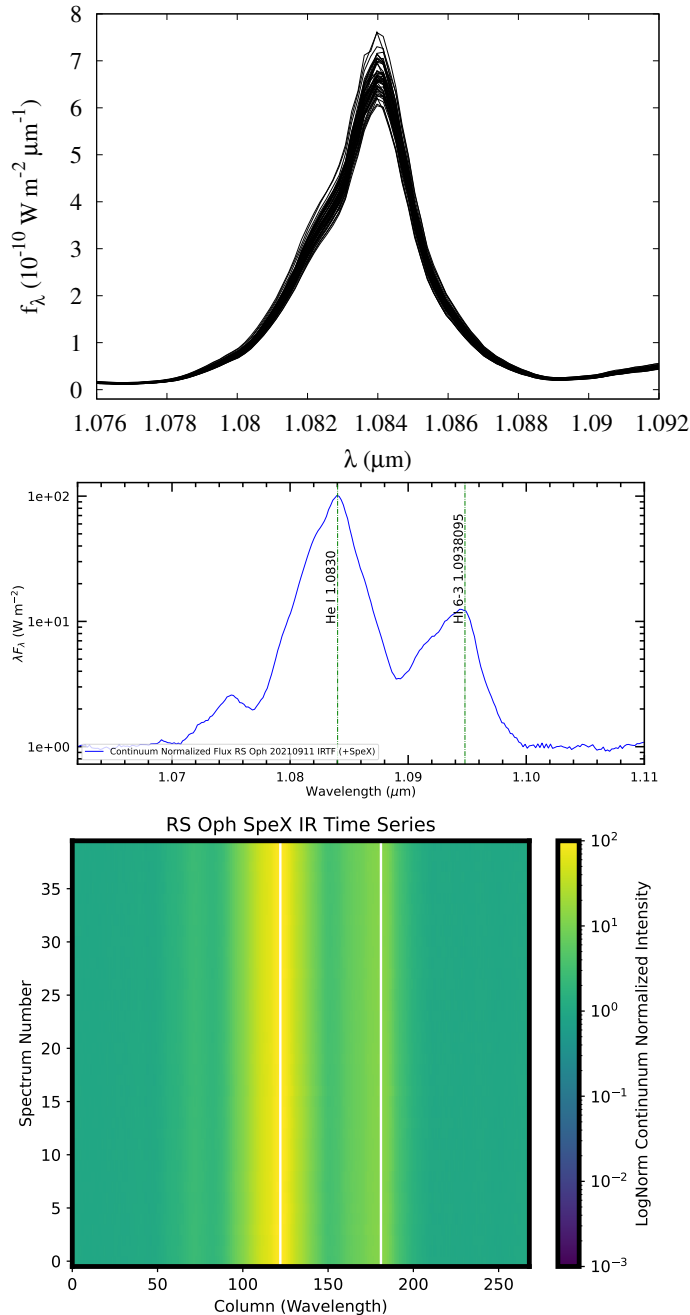


**Figure 8.** Top: Profile of the He I triplet during high cadence observations. Fluxes are as observed, and all high cadence data are shown. Middle: Example of continuum normalised spectrum in the region of interest near the He I line. Bottom: Three-dimensional rendering of the time series spectra obtained on a  $\sim 6\text{s}$  cadence over a  $\sim 240\text{s}$  interval on day 31.5. The vertical white line at column 122, corresponds to the wavelength of He I, while the vertical white line at column 181 is H I 6–3 line at  $1.0938 \mu\text{m}$ . The flux scaling uses a LogNormal rendering as indicated by the intensity bar to the right of the panel. Time scale starts at the bottom and increases upwards.

(ii) during the eruption, there is evidence for a (relatively) cool gas at  $8900 \text{ K}$ , resulting from flash-ionisation of the red giant wind by hard radiation from the eruption;

(iii) there are several coronal emission lines in the NIR during the first month of the eruption; the implied temperature of the coronal gas is  $\sim 10^6 \text{ K}$ ;

(iv) there is no evidence for rapid variability in the He I  $1.0833 \mu\text{m}$  line during the SSS phase.

## ACKNOWLEDGEMENTS

We thank the referee for their very careful and thorough review; their comments have resulted in considerable improvements to the paper. This paper is based on observations obtained under IRTF program 2021A012, and 2022A04, and the authors thank the IRTF staff for their assistance at the telescope. CEW acknowledges support from NASA. SS acknowledges partial support from a NASA Emerging Worlds grant to ASU (80NSSC22K0361), as well as support from his ASU Regents Professorship. KLP acknowledges support from the UK Space Agency. We acknowledge with thanks the variable star observations from the *AAVSO International Database* contributed by observers worldwide and used in this research.

## DATA AVAILABILITY

The IRTF data are available from the IRTF archive [http://irtfweb.ifa.hawaii.edu/research/irtf\\_data\\_archive.php](http://irtfweb.ifa.hawaii.edu/research/irtf_data_archive.php). The Swift data are available from [https://www.swift.ac.uk/swift\\_live](https://www.swift.ac.uk/swift_live).

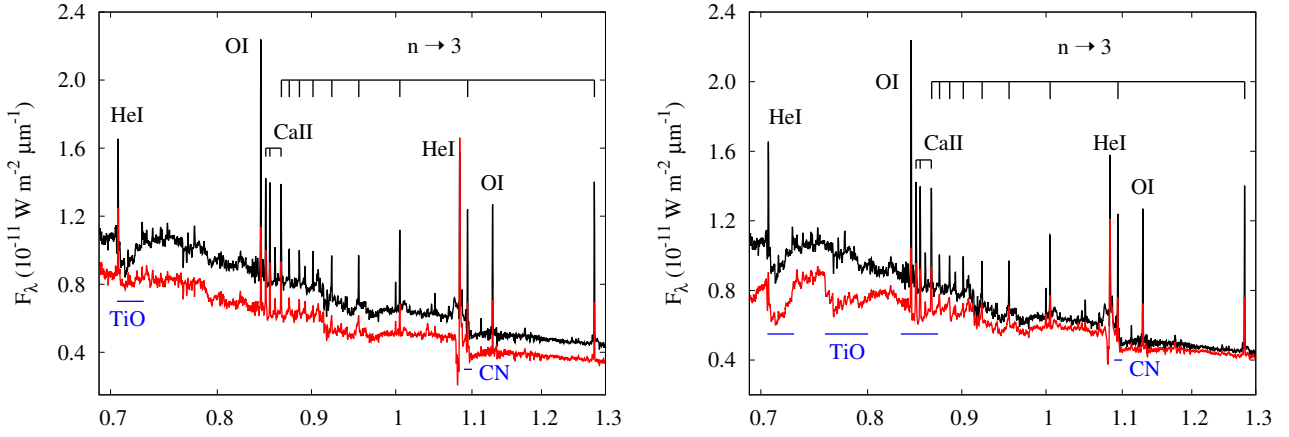


**Figure 9.** Left: pre-eruption (day  $-428.1$ , black) and post-eruption (day  $335.3$ , red) spectra in the  $0.69\text{--}1.3\ \mu\text{m}$  range. Right: pre-eruption (day  $-428.1$ , black) and post-eruption (day  $624.1$ , red) spectrum. In both panels, key emission lines and molecular features are identified, and the wavelength scales are logarithmic to stretch out the shortest wavelengths.

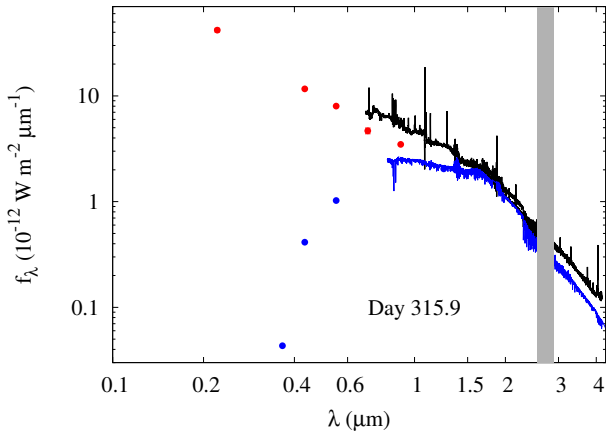


**Figure 10.** Day 315 spectrum of *RS Oph* (black curve), with Swift UVOT and *BVRI* photometry (red points; error bars are smaller than the plotted points). *RS Oph* data dereddened by  $E(B - V) = 0.73$ . Blue spectrum is that of *HD120052*, together with *UBVR* photometry (cf. Fig. 2). Grey block indicates wavelength region over which the atmospheric transmission is poor.

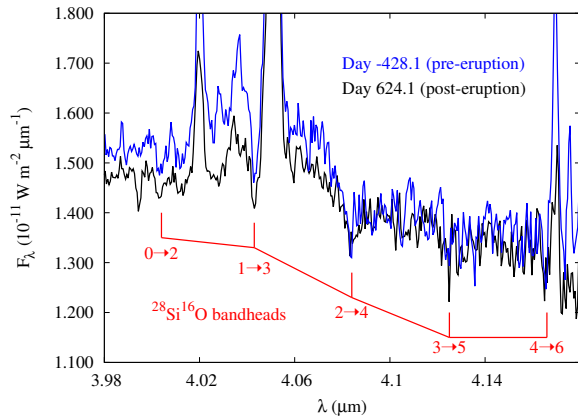


**Figure 11.** The IRTF spectra in the region of the first overtone *SiO* bands (marked in red).

## REFERENCES

- Abe K., et al., 2025, *A&A*, 695, A152
- Anupama G. C., Mikołajewska J., 1999, *A&A*, 344, 177
- Anupama G. C., 2008, in *RS Ophiuchi (2006) and the Recurrent Nova Phenomenon*, *Astronomical Society of the Pacific Conference Series*, eds A. Evans, M. F. Bode, T. J. O'Brien, M. J. Darnley, vol. 401, p. 31, San Francisco
- Arnaud M., Rothenflug R., 1985, *A&AS*, 60, 425
- Asplund M., Amarsi A. M., Grevesse N., 2021, *A&A*, 653, A141
- Azzollini A., Shore S. N., Kuin P., Page K. L., 2023, *A&A*, 674, A139
- Badnell N. R., et al., 2006, in *IAU Symposium 234, Planetary Nebulae in our Galaxy and Beyond*, ed. M. J. Barlow & R. H. Méndez (Cambridge: Cambridge University Press), 211
- Baker J. G., Menzel D. H., 1938, *ApJ*, 88,52
- Banerjee D. P. K., Das R. K., Ashok N. M., 2009, *MNRAS*, 399, 357
- Banerjee D. P. K., et al., 2023, *ApJ*, 954, L16
- Barry R. K., Mukai K., Sokoloski J. L., Danchi W. C., Hachisu I., Evans A., Gehrz R. D., Mikołajewska J., 2008, in *Evans A., Bode M. F., O'Brien T. J., Darnley M. J., eds, Astronomical Society of the Pacific Conf. Ser. Vol. 401, RS Ophiuchi (2006) and the Recurrent Nova Phenomenon*. *Astron. Soc. Pac.*, San Francisco, p. 52
- Beardmore A. P., Osborne J. P., Page K. L., Goad M. R., Bode M. F., Starrfield S., 2008, in *Evans A., Bode M. F., O'Brien T. J., Darnley M. J., eds, Astronomical Society of the Pacific Conf. Ser. Vol. 401, RS Ophiuchi (2006) and the Recurrent Nova Phenomenon*. *Astron. Soc. Pac.*, San Francisco, p. 296
- Beck S., 2021, *AAVSO Alert Notice #752*
- Bell G. S., Berry D. S., Graves S. F., Currie M. J., Draper P. W., 2024, in *Astronomical Data Analysis Software and Systems XXXI*, eds B. V. Hugo, R. Van Rooyen, O. M. Smirnov, *Astronomical Society of the Pacific Conference Series*, 535, 455
- Bhatia A. K., Kastner S. O., 1995, *ApJS*, 96, 325
- Bode M. F., Kahn F. D., 1985, *MNRAS*, 217, 205
- Bode M. F., 1987, editor, *RS Ophiuchi (1985) and the recurrent nova phenomenon*, *VNU Science Press, Utrecht*
- Bode M. F., et al., 2006, *IAUC #8761, #1*
- Boffin H., Merc J., 2025, *A&A*, 701, A151
- Bollimpalli D. A., Hameury J.-M., Lasota J.-P., 2018, *MNRAS*, 481, 5422
- Bowen I. S., 1947, *PASP*, 59, 196
- Brandi E., Quiroga C., Mikołajewska J., Ferrer O. E., García L. G., 2009, *A&A*, 497, 815
- Breeveld A. A., Landsman W., Holland S. T., Roming P., Kuin N. P. M., Page M. J., 2011, in *Gamma Ray Bursts*, ed J. E. McEnery, *American Institute of Physics Conference Proceedings*, Vol. 1358, 373
- Cardelli J. A., Clayton G. C., Mathis J. S., 1989, *ApJ*, 345, 245
- Cheung C. C., et al., 2025, *ApJ*, 935, 44
- Chomiuk L., Metzger B. D., Shen K. J., 2021, *ARA&A*, 59, 391
- Cox A. N., 2000, *Allen's Astrophysical Quantities*, 4th edition. *AIP Press; Springer, New York*
- Currie M. J., Berry D. S., jennes T., Gibb A. G., Bell G. S., Draper P. W., 2014, in *Astronomical Data Analysis Software and Systems XXIII*. eds N. Manset, P. Forshay, *Astronomical Society of the Pacific Conference Series*, vol 485, p.391
- Cushing M. C., Vacca W. D., Rayner J. T., 2004, *PAstronomical Society of the Pacific*, 116, 362
- Cushing M. C., Rayner J. T., Vacca W. D., 2005, *ApJ*, 623, 1115
- Das R., Banerjee D. P. K., Ashok N. M., 2006, *ApJ*, 653, L141
- de Ruiter I., Nyamai M. M., Rowlinson A., Wijers R. A. M. J., O'Brien T. J., Williams D. R. A., Woudt P., 2023, *MNRAS*, 523, 132
- Eggleton P. P., 1983, *ApJ*, 268, 368
- Evans A., Callus C. M., Albinson J. S., Whitelock P. A., Glass I. S., Carter B., Roberts G., 1988, *MNRAS*, 234, 755
- Evans A., et al., 2007a, *MNRAS*, 374, L1
- Evans A., et al., 2007b, *ApJ*, 663, L29
- Evans A., et al., 2007c, *ApJ*, 671, L157
- Evans A., Bode M. F., O'Brien T. J., Darnley M. J., 2008 editors, *RS Ophiuchi (2006) and the Recurrent Nova Phenomenon*, *Astronomical Society of the Pacific Conference Series*, Vol. 401, San Francisco
- Evans A., Geballe T. R., Woodward C. E., Banerjee D. P. K., Gehrz R. D., Starrfield S., Shahbandeh M., 2022, *MNRAS*, 517, 6077
- Evans A., et al., 2023, *MNRAS*, 522, 4841
- Geary K., Amorim A., 2021, *CBET #5013*
- Gehrels N., et al., 2004, *ApJ*, 611, 1005
- Gehrz R. D., et al., 2008, *ApJ*, 627, 1167
- Greenhouse M. A., Grasdalen G. L., Woodward C. E., Benson J., Gehrz R. D., Rosenthal E., Skrutskie M. F., 1990, *ApJ*, 352, 307
- Habtie G. R., Das R., 2025, *MNRAS*, 537, 2046
- Helton L. A., et al., 2012, *ApJ*, 755, 37
- Herbig G. H., Soderblom D. R., 1980, *ApJ*, 242, 628
- Hummer D. G., et al., 1993, *A&A*, 279, 298
- Islam N., Mukai K., Sokoloski J. L., 2024, *ApJ*, 960, 125
- Karzas W. J., Latter R., 1961, *ApJS*, 6, 167
- Kastner S. O., Bhatia A. K., 1995, *ApJ*, 439, 346
- Lico R., et al., 2024, *A&A*, 692, A107
- Merc J., Boffin H., 2025, *A&A*, 695, A61
- Merc J., et al., 2025, *MNRAS*, 541, L14
- Mikołajewska J., Shara M. M., 2017, *ApJ*, 847, 6
- Munari U., Tabacco F., 2022, *RNAAS*, 6,103
- Munari U., Valisa P., 2021, *arXiv:2109.01101*
- Munari U., Valisa P., 2022, *arXiv:2203.01378*
- Munrai U., Giroletti M., Marcote B., O'Brien T. J., Veres P., Yang J., Williams D. R. A., Woudt P., 2022, *A&A*, 666, L6
- Mürset U., Schmid H. M., 1999, *A&AS*, 137, 473
- Nayana A. J., et al., 2024, *MNRAS*, 528, 5528
- Nelson T., Orio M., Cassinelli J. P., Still M., Leibowitz E., Mucciarelli P., 2008, *ApJ*, 673, 1067
- Ness J.-U., et al., 2024, *A&A*, 670, A131
- Nikolov Y., Luna G. J. M., Stoyanov K. A., Borisov G., Mukai K., Sokoloski J. L., 2023, *A&A*, 679, A150
- Orio M., et al., 2022, *ApJ*, 938, 34
- Orio M., et al., 2023, *ApJ*, 955, 37
- Osborne J. P., et al., 2011, *ApJ*, 727, 124
- Osterbrock D. E., Ferland G. J., 2006, *Astrophysics of Gaseous Nebulae and Active Galactic Nuclei*, 2nd edition, *Univ. Sci. Books, Sausalito, California*
- Page K. L., et al., 2022, *MNRAS*, 514, 1557
- Pavlenko Ya. V., et al., 2008, *A&A*, 485, 541
- Pavlenko Ya. V., Woodward C. E., Rushton M. T., Kaminsky B., Evans A., 2010, *MNRAS*, 404, 206
- Pavlenko Ya. V., Kaminsky B., Rushton M. T., Evans A., Woodward C. E., Helton L. A., O'Brien T. J., Jones D., Elkin V., 2016, *MNRAS*, 456, 181
- Pavlenko Ya. V., Evans A., Banerjee D. P. K., Geballe T. R., Munari U., Gehrz R. D., Woodward C. E., Starrfield S., 2016, *MNRAS*, 456, 181
- Persson S. E., 1988, *PASP*, 100, 710
- Phan V. H. M., Cristofari P., Peretti E., Tatischeff V., Ciardi A., 2025, *arXiv:2504.02043*
- Planquart L., Jorissen A., Van Winckel H., 2025, *A&A*, 694, A85
- Rayner J. T., et al., 2003, *PASP*, 115, 362
- Rayner J. T., Cushing M. C., Vacca W. D., 2009, *ApJS*, 185, 289
- Rudy R. J., Dimpfl W. L., Lynch D. K., Mazuk S., Venturini C. C., Wilson J. C., Puetter R. C., Perry R. B., 2003, *ApJ*, 596, 1229
- Rushton M. T., et al., 2010, *MNRAS*, 401, 99
- Rushton M. T., Woodward C. E., Gehrz R. D., Evans A., Kamin-

- sky B., Pavlenko Ya. V., Eyres S. P. S., 2022, *MNRAS*, 517, 2526
- Schaefer B. E., 2022, *MNRAS*, 517, 6150
- Schaefer B. E., 2023, *MNRAS*, 524, 3146
- Shore S. N., Kenyon S. J., Starrfield S., Sonneborn G., 1996, *ApJ*, 456, 717
- Snijders M. A. J., 1987, *Ap&SpSci*, 130, 243
- Somero A., Hakala P. Wynn G. A., 2017, *MNRAS*, 464, 2784
- Starrfield S., et al., 2025, *ApJ*, 982, 89
- Storey P. J., Hummer D. G., 1995, *MNRAS*, 272, 41
- Taguchi K., Ueta T., Isogai K., 2021, *ATel* #14838
- Tomov N. A., et al., 2023, *A&A*, 671, A49
- van Belle G. T., et al., 1999, *AJ*, 117, 521
- van Hoof P. A. M., 2018, *Galaxies*, 6, 63
- Walder R., Folini D., Shore S. N., 2008, *A&A*, 484, L9
- Wood B. E., Müller H.-R., Harper G. M., 2016, *ApJ*, 829, 74
- Woodward, C. E., Helton L. A., Evans, A., van Loon J. Th., 2008, in Evans A., Bode M. F., O'Brien T. J., Darnley M. J., eds, *Astronomical Society of the Pacific Conf. Ser. Vol. 401, RS Ophiuchi (2006) and the Recurrent Nova Phenomenon*. Astron. Soc. Pac., San Francisco, p. 260
- Woodward C. E., Banerjee D. P. K., Geballe T. R., Page K. L., Starrfield S., Wagner R. M., 2021, *ApJ*, 922, L10
- Worters H. L., Eyres S. P. S., Bromage G. E., Osborne J. P., 2007, *MNRAS*, 379, 1557
- Wynn G., 2008, in Evans A., Bode M. F., O'Brien T. J., Darnley M. J., eds, *Astronomical Society of the Pacific Conf. Ser. Vol. 401, RS Ophiuchi (2006) and the Recurrent Nova Phenomenon*. Astron. Soc. Pac., San Francisco, p. 73

**APPENDIX A: EMISSION LINE FLUXES**

**Table A1.** Dereddened line fluxes. Where the line structure is complex, fluxes are listed for the strongest, central, component. Fluxes, in  $\text{W m}^{-2}$ , are given in the form  $X.YZ(-EE) = X.YZ \times 10^{-EE}$ . Upper limits are  $3\sigma$ .

20200610	20210820	20210911	20220516	20220620	20220710	20230424	ID	$\lambda$
-428.1	11.7	31.7	281.1	315.9	335.3	624.1		( $\mu\text{m}$ )
3.33(-15)		2.93(-13)	5.06(-15)	3.46(-15)	2.93(-15)	1.64(-15)	He I	0.7067
< 4.5(-16)	1.68(-14)	1.61(-14)	< 5.1(-16)	< 3(-15)	< 1.2(-15)		[S XII]	0.7613
1.31(-15)	4.79(-13)						O I	0.7776
	1.54(-13)	6.16(-14)	< 5.7(-16)	3.80(-16)	< 1.2(-15)		[Fe XI]	0.7894
1.01(-14)	3.91(-12)	1.00(-12)	4.19(-15)	4.59(-15)	3.77(-15)	4.82(-15)	O I	0.8449
4.91(-15)	2.48(-13)	5.84(-14)	3.37(-15)	3.97(-15)	3.41(-15)	4.44(-15)	Ca II	0.8500
4.33(-15)	1.87(-13)	2.97(-14)	2.15(-15)	3.74(-15)	2.43(-15)	3.48(-15)	Ca II	0.8544
4.67(-15)	5.63(-13)	1.25(-13)	2.97(-15)	3.79(-15)	3.08(-15)	3.51(-15)	Ca II	0.8665
	2.74(-13)	6.18(-14)	< 6.3(-16)	3.90(-16)*	< 1.1(-15)		[S IX]	0.9391
	1.80(-15)	6.08(-14)	1.03(-15)*	< 5.4(-16)	< 3.6(-17)		[S VIII]	0.9914
4.19(-15)	9.69(-13)	1.84(-13)	2.61(-15)	2.21(-15)	1.75(-15)	2.44(-15)	H I 7-3	1.0052
	< 5.4(-15)	1.84(-13)	3.04(-15)*				[Ar XIII]	1.0143
		7.08(-15)	3.92(-16)	3.87(-16)			[P XI]	1.031
	4.33(-13)	2.53(-14)	< 2.5(-16)	< 1.6(-15)	< 5.4(-16)		[Fe XIII]	1.075
8.59(-15)		3.40(-12)	2.52(-14)	1.69(-14)	1.37(-14)	1.09(-14)	He I	1.0833
5.77(-15)	2.71(-12)	5.54(-13)	2.16(-15)	3.09(-15)	2.76(-15)	4.04(-15)	H I 6-3	1.0941
7.10(-15)	2.36(-12)	5.63(-13)	3.94(-15)	3.17(-15)	2.81(-15)	4.19(-15)	O I	1.129
1.70(-16)	9.30(-14)	5.37(-14)	3.72(-16)	1.65(-16)	< 3(-16)	3.37(-16)	[S IX]	1.2535
				3.66(-16)			[P VIII]	1.2784
	< 1.4(-13)	< 2.4(-15)			5.46(-16)		[Cr IX]	1.2786
9.70(-15)	2.36(-12)	4.75(-13)	4.66(-15)	4.39(-15)	3.60(-15)	5.42(-15)	H I 5-3	1.2822
3.42(-16)	8.17(-14)	5.88(-14)					O I	1.3168
< 3.3(-16)	< 1.5(-14)	2.47(-14)	< 4.6(-16)	< 5.7(-16)		< 7.5(-16)	[Si X]	1.4309
< 3.3(-16)	< 1.4(-14)		< 1.1(-15)	< 4.8(-16)	< 2.2(-16)	< 5.7(-16)	[Si IX]	1.5599
		3.08(-14)	4.81(-16)	4.53(-16)	3.64(-16)	< 5.7(-16)	[P VIII]	1.7361
1.44(-15)	1.45(-13)	1.73(-14)				6.27(-16)	H I 9-4	1.8179
8.39(-15)	3.80(-12)	1.09(-12)	4.39(-15)	4.67(-15)		5.64(-15)	H I 4-3	1.8755
3.89(-16)	2.84(-13)	4.69(-14)				3.66(-16)	H I 8-4	1.9461
8.75(-16)	< 2.1(-15)	3.56(-14)	< 4.6(-16)	< 8.4(-16)	< 3.6(-17)	4.28(-16)	[Si VI]	1.965
	2.46(-14)	2.62(-15)		< 3.6(-16)	< 1.4(-16)	< 1.5(-16)	[Al IX]	2.045
7.67(-16)	3.89(-13)	6.33(-14)	7.05(-16)	2.77(-16)	< 1.4(-16)	7.45(-16)	He I	2.0587
1.51(-15)	2.90(-13)	6.57(-14)	8.04(-16)	6.83(-16)	5.83(-16)	8.86(-16)	H I 7-4	2.1661
	< 8.4(-16)	3.30(-16)	< 2.6(-16)		< 2.0(-16)	< 2.3(-16)	[Ca VIII]	2.321
< 3.6(-16)	9.24(-16)	1.81(-14)	< 2.5(-16)	< 3.0(-16)		< 2.3(-16)	[Si VII]	2.4833

\*The measured wavelength is not a good match to the line wavelength.

**Table A1.** Continued. Dereddened line fluxes. Fluxes, in  $\text{W m}^{-2}$ , are given in the form  $X.YZ(-EE) = X.YZ \times 10^{-EE}$ . Upper limits are  $3\sigma$ .

20200610 -428.1	20210820 11.7	20210911 31.7	20220516 281.1	20220620 315.9	20220710 335.3	20230424 624.1	ID	$\lambda$ ( $\mu\text{m}$ )
	2.63(-14)	†			†	< 7.7(-17)	H I 16-5	2.5261
	4.69(-14)	†			†	< 7.6(-17)	H I 11-5	2.873
	< 3.3(-15)	†	< 1.0(-16)	< 1.7(-16)	†	< 2.3(-14)	[Al v]	2.9052
	< 2.2(-15)	†		< 1.4(-16)	†	< 1.8(-16)	[Mg VIII]	3.028
5.83(-16)	7.80(-14)	†		2.16(-16)	†	< 1.8(-16)	H I 10-5	3.0392
	< 1.3(-15)	†	< 7.5(-17)	< 1.5(-16)	†	< 1.8(-16)	[Ca IV]	3.2067
8.14(-16)	9.64(-14)	†		2.32(-16)	†	3.69(-16)	H I 9-5	3.297
	2.63(-16)	†	< 2.2(-17)	< 3.0(-17)	†	< 1.6(-17)	[Al VI]	3.6597
	1.73(-15)	†			†		[Al VIII]	3.69
1.30(-16)		†			†	1.20(-16)	H I 19-6	3.64593
1.18(-16)	2.01(-14)	†			†	9.30(-17)	H I 18-6	3.6926
1.60(-16)		†			†		H I 17-6	3.7494
4.34(-16)	1.42(-13)	†			†	2.56(-16)	H I 8-5	3.7406
1.49(-16)		†			†		H I 16-6	3.81945
1.52(-16)		†			†		H I 15-6	3.90755
2.61(-17)	4.58(-16)	†	3.04(-17)	4.67(-17)	†	< 1.6(-17)	[Si IX]	3.9357
1.62(-15)	5.32(-13)	†	7.55(-16)	7.07(-16)	†	8.96(-16)	H I 5-4	4.0523

\*The measured wavelength is not a good match to the line wavelength.

†Wavelength not covered.

This paper has been typeset from a  $\text{\TeX}/\text{\LaTeX}$  file prepared by the author.